Nanoscale

Accepted Manuscript

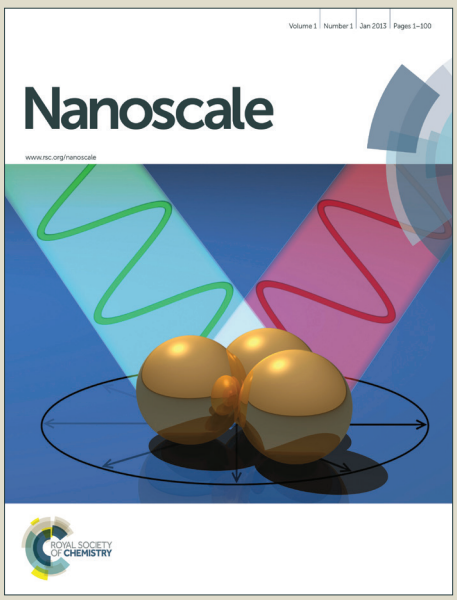

ROYAL SOCIETY OF CHEMISTRY

www.rsc.org/nanoscale

Nanoscale

Dynamic Article Links ►

Cite this: DOI: 10.1039/c0xx00000x

www.rsc.org/xxxxxx

COMMUNICATION

Cytotoxicity, tumor targeting and PET imaging of sub-5 nm $KGdF_4$ multifunctional rare earth nanoparticles†

Xinmin Cao,[a] Fengwen Cao,[a] Liqin Xiong,*[ab] Yang Yang,[c] Tianye Cao,[d] Xi Cai,[a] Wangxi Hai,[b] Biao Li,[b] Yixiao Guo,[a] Yimin Zhang,[a] and Fuyou Li [c]

Received (in XXX, XXX) Xth XXXXXXXXX 20XX, Accepted Xth XXXXXXXXX 20XX
DOI: 10.1039/b000000x

Ultrasmall sub-5 nm $KGdF_4$ rare earth nanoparticles were synthesized as multifunctional probes for fluorescent, magnetic, and radionuclide imaging. The cytotoxicity of these nanoparticles in human glioblastoma U87MG and human non-small cell lung carcinoma H1299 were evaluated, and their application for *in vitro* and *in vivo* tumor targeted imaging has also been demonstrated.

Rare earth nanoparticles (REs) have recently attracted enormous attention in the field of biological imaging owing to their unique optical properties, such as narrow emission bandwidths, large Stokes shifts, long fluorescence lifetimes and photostability.[1-6] In particular, REs can be excited with near-infrared (NIR) to emit in both the visible and infrared region of the electromagnetic spectrum, through the up-conversion and down-conversion process, respectively. Up-conversion luminescence occurs during the excitation of trivalent rare earth ions by the sequential absorption of two or more NIR photons, and such a unique luminescent mechanism excludes both conversional luminescent labels and endogenous fluorescent substances. REs are also capable of generating short-wavelength infrared emissions (SWIR, 1,000~2,300 nm) with large Stokes shifts after NIR excitation through down-conversion fluorescence mechanisms.[6]

Furthermore, REs are also useful for multimodal *in vivo* imaging because simple variations in the composition of the lattice atoms and dopant ions integrated into the REs can be easily implemented, yielding various distinct biomedical activities relevant to magnetic resonance imaging (MRI), computed tomography (CT), positron emission tomography (PET), single-photon emission computed tomography (SPECT), and photoacoustic imaging.[7-13] These multiple functions embedded in a single type of REs play a crucial role in precise disease diagnosis. Especially, with their increasing bioapplications, the potential dissemination of REs and their interactions in the human body have increased.[14-16] The studies on the toxicity of REs were mostly limited to $NaMF_4$, ($M = Y^{3+}$, Gd^{3+}, Lu^{3+}) hosts. The previous results demonstrated that those REs exhibited a low toxicity effect on cells and animals in most cases.[17-19] However, there are few reports on the toxicity of REs based on $KGdF_4$ host.[20,21]

In addition, the particle size is a key factor requiring consideration to realize the application of REs in biomedical imaging. Current REs are typically larger than 10 nm, which is not optimal for using as bioimaging probes. It is recently demonstrated that the nanoparticles with size less than 10 nm are easily taken up and excreted, and show longer blood circulation times in comparison with larger ones.[22-25] However, the size of particle and the upconversion emission intensity are mutually dependent parameters, and in general a smaller nanoparticle size will result in the weaker emission. So it is a big challenge to test *in vivo* behavior of ultrasmall sub-5nm REs by optical imaging technology. To overcome this deficiency, herein, PET is chosen to detect the *in vivo* biodistribution and tumor imaging of ultrasmall REs because it shows no limited tissue penetration compared with fluorescent imaging and exhibits higher sensitivity than both MRI and CT.

In this work, we report REs based on $KGdF_4$ host as nanoprobes for *in vitro* and *in vivo* tumor imaging for the first time. The prepared $KGdF_4$ REs were sub-5 nm in diameter, exhibited the up/down-conversion luminescence by doped Yb^{3+}/Tm^{3+} and Eu^{3+}, respectively. Moreover, these REs were applied to target imaging human glioblastoma U87MG cells by conjugated with RGD peptide, and no obvious cytotoxicity were detected. Furthermore, to visualize *in vivo* behavior of $KGdF_4$ by PET imaging, $^{18}F^-$ was labeled with $KGdF_4$, and $^{18}F^-$ labeled $KGdF_4$ REs were able to imaging U87MG and H1299 tumors in living mice after intravenous injection.

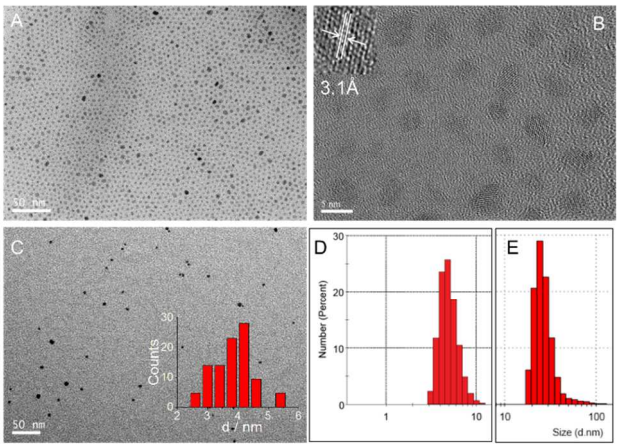

Fig. 1 Transmission electron microscopy (TEM) images of the $KGdF_4$ REs. **A**, OA-capped $KGdF_4$ REs. **B**, high resolution TEM of OA-capped $KGdF_4$ sample. **C**, PAA-coated $KGdF_4$ REs, inset, the average diameter of the $KGdF_4$ REs obtained from the TEM result. **D**, dynamic light scattering (DLS) of the OA-capped $KGdF_4$ REs. **E**, DLS of the PAA-coated $KGdF_4$ REs.

The $KGdF_4$ host possesses several attractive merits as multifunctional REs such as the tendency to form ultrasmall size nanoparticles (~10 nm), the absence of phase change down to ~3.7 nm, and the intrinsic magnetic and luminescent properties. [26] Therefore, we choose $KGdF_4$ as a host to obtain the ultrasmall sub-5 nm multifunctional REs. Oleic acid (OA)-capped $KGdF_4$ REs was synthesized by a modified hydrothermal route. Due to the presence of oleic acid on the surface of $KGdF_4$ REs, the $KGdF_4$-OA sample was well dispersed in nonpolar solvent such as cyclohexane, chloroform, and dichloromethane. Therefore, surface functionalization of OA-capped $KGdF_4$ REs is required prior to the biological applications. Herein, using PAA coating methods by a modified ligand exchange procedure, hydrophobic $KGdF_4$-OA was easily converted into hydrophilic ones. Following the exchange with oleic acid, the resultant PAA-conjugated $KGdF_4$ possessed two properties: (I) good dispersibility in aqueous solutions, and (II) carboxyl functional groups on the surface of REs to allow conjugation with biological molecules (such as peptides) for further targeted *in vitro* and *in vivo* studies.

As shown in **Fig.1**, transmission electron microscopy (TEM) images showed that the $KGdF_4$ REs were quite monodispersed with an average diameter of 3.79 nm. High-resolution TEM image suggested that the $KGdF_4$ REs was a single crystal with an interplanar spacing of 3.1Å, which could be indexed as the *d* spacing for the (110) lattice planes. Furthermore, the energy-dispersive X-ray analysis (EDXA) patterns confirmed the presence of K, Gd, and F elements in the as-synthesized samples (**Fig.S1**). The crystal structure of the as-synthesized $KGdF_4$ REs was identified using powder X-ray diffraction (XRD) analysis (**Fig.S2**). The broad XRD peaks imply that particles obtained fall within the nano domain. Although XRD peak intensities are very weak, the crystal phase could still be identified. The XRD patterns could be indexed as the cubic phase of $NaGdF_4$ (JCPDS No. 27-0697), which was in good agreement with that reported by Capobianco et al.[26] The dynamic light scattering (DLS) measurement indicated that the effective hydrodynamic diameter of the OA-capped $KGdF_4$ REs was ~4.9 nm (**Fig. 1D**). After PAA coating, FTIR spectrum showed the stretching mode of the –COOH group at 1727 cm^{-1}, suggesting PAA bond to the particle surface (**Fig. S3**). And the effective hydrodynamic diameter of the PAA-coated $KGdF_4$ REs reached ~30 nm (**Fig. 1E**). This increase in hydrodynamic diameter was attributed to the linkage of the PAA polymer to the surface of $KGdF_4$ REs. The zeta potential of the PAA-coated $KGdF_4$ REs in water was about -13 mV (**Fig. S4**). Thermogravimetry analysis (TGA) showed that percentage of PAA on the $KGdF_4$ REs was approximately 13% (**Fig. S5**). In addition, DLS analysis exhibited that PAA-coated $KGdF_4$ REs were stable in water for weeks without aggregation (**Fig. S6**).

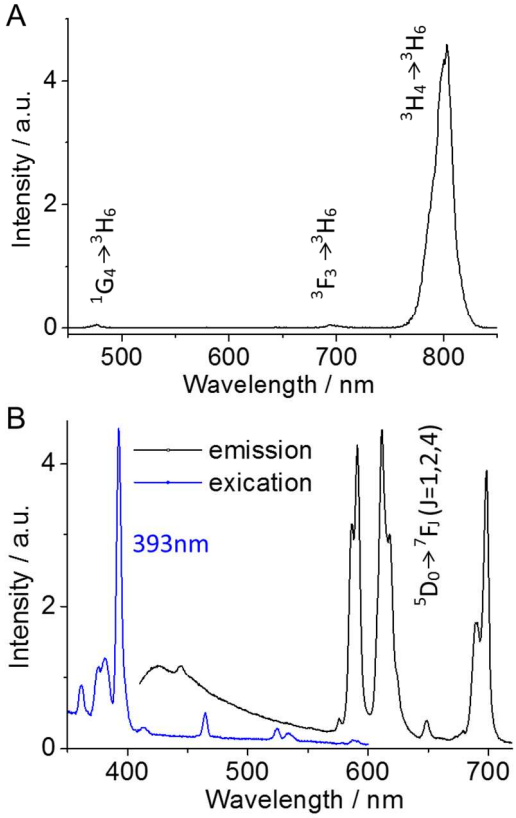

Fig. 2 A, Up-conversion luminescence spectrum of the OA-capped $KGdF_4$:Yb^{3+}, Tm^{3+} REs. **B,** Excitation and emission spectra of the OA-capped $KGdF_4$:Eu^{3+} REs.

Up/down-conversion luminescence of $KGdF_4$ REs were obtained by doped Yb^{3+}/Tm^{3+} and Eu^{3+}, respectively. As shown in **Fig. 2**A, under excitation of CW laser at 980 nm, the up-conversion luminescence spectrum of the $KGdF_4$:Yb^{3+}, Tm^{3+} sample exhibited three Tm^{3+} emission bands. The up-conversion luminescence bands at 476, 694 and 803 nm originated from $^1G_4$–$^3H_6$, $^3F_3$–$^3H_6$ and $^3H_4$–$^3H_6$ transitions of Tm^{3+}, respectively.

The down-conversion luminescence properties of the $KGdF_4$:Eu^{3+} were characterized by excitation and emission spectra (**Fig. 2**B). The excitation spectra consisted of the characteristic absorption peaks of Eu^{3+} corresponding to the direct excitation from the europium ground state into the higher

excited states of the Eu^{3+} f-electrons. The most intense peak was centered at 393 nm, which can be assigned to the $^7F_0$–$^5L_6$ transitions of Eu^{3+} ions. Under excitation at 393 nm, the emission spectra were composed of three strong emission peaks at about 591 nm, 611 nm, and 698 nm, which can be attributed to the $^5D_0$–^7F_J (J = 1, 2, 4) transition lines of the Eu^{3+} ions, respectively. The intensity of electric dipole transition ($^5D_0$–$^7F_2$) at 611 nm was slightly higher than that of magnetic dipole transition ($^5D_0$–$^7F_1$) at 591 nm.

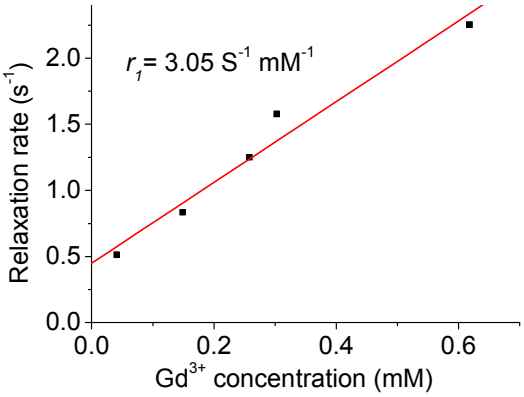

Fig. 3 ^{1}H spin−lattice relaxation rates ($1/T_1$) of H_2O as a function of molar concentration (mM) of $KGdF_4$ REs at 1.5 T.

The longitudinal relaxation time (T_1) was measured in aqueous solutions with different Gd^{3+} concentrations. To evaluate the ionic relaxivities, the Gd^{3+} concentration of the $KGdF_4$ REs was determined using ICP-MS, after digesting the $KGdF_4$ REs in concentrated nitric acid. From the slope of the plot of $1/T_1$ versus the Gd^{3+} concentration (**Fig. 3**), the ionic longitudinal relaxivity (r_1) was determined to be 3.05 ± 0.32 S^{-1}·mM^{-1}.

The cytotoxicity of the $KGdF_4$ REs was evaluated by the CCK-8 assay in human non-small cell lung carcinoma H1299 and human glioblastoma U87MG (**Fig. 4**). The viability of cells above a 10–1000 μg/mL concentration of $KGdF_4$ REs was slightly decreased, and the difference was statistically significant. After 12 h of incubation with $KGdF_4$ REs, the cellular viability were estimated to be greater than 96% for both cell lines. After 24 h of incubation with $KGdF_4$ REs, cells maintained greater than 94% and 88% cell viabilities for H1299 and U87MG cells, respectively. Even after 48 h of incubation with $KGdF_4$ REs, more than 76% of H1299 cells and 62% of U87MG cells were viable, respectively. These results demonstrated the weak toxic effects of $KGdF_4$ REs on cell viability in these conditions.

Integrin $\alpha_v\beta_3$ plays a pivotal role in tumor angiogenesis and is a receptor for the extracellular matrix proteins with the exposed RGD tripeptide sequence.[3,27,28] Herein, c(RGDFK) was chosen as target ligand for further application in targeted imaging of cancer cells based on $KGdF_4$:Eu^{3+} REs. The covalent coupling of c(RGDFK) to the surface of PAA-coated $KGdF_4$:Eu^{3+} REs was facilitated by EDC, which activated the carboxyl groups of $KGdF_4$:Eu^{3+} REs and led to the formation of amide bonds. To evaluate the $\alpha_v\beta_3$ integrin specificity of the RGD-conjugated $KGdF_4$:Eu^{3+} REs, U87MG cells (expressing high levels of integrin $\alpha_v\beta_3$) were chosen for target-specific imaging, whereas H1299 cells (expressing low levels of integrin $\alpha_v\beta_3$) was used in the control experiments. The living cells were incubated with $KGdF_4$:Eu^{3+} REs (~20 μg/mL) for 2 h at 37 °C. Cell imaging was then performed by confocal luminescence microscopy. As shown in **Fig. 5B**, intense red luminescence signal were detected within the U87MG cells after 2 h of incubation with RGD-conjugated $KGdF_4$:Eu^{3+} REs at 37 °C, and no aggregation of REs was observed. Bright-field measurements after treatment with $KGdF_4$:Eu^{3+} REs confirmed that the cells were viable throughout the imaging experiments. In contrast, probe controls (PAA-coated $KGdF_4$:Eu^{3+} REs) showed weak luminescence emission (**Fig. 5A**). In addition, the luminescence signal of RGD-conjugated $KGdF_4$:Eu^{3+} REs was mainly observed in the cytoplasm region of the U87MG cells (**Fig. 5B**), while the luminescence signal of PAA-coated $KGdF_4$:Eu^{3+} REs was mainly detected on the cell membrane (**Fig. 5A**). Integrin receptor specific of $KGdF_4$:Eu^{3+} REs was further carried out by cell control assay, slightly weaker luminescence signals were detected in the control H1299 cells (**Fig. 5C, D**) compared with that detected in the U87MG cells after RGD-conjugated $KGdF_4$:Eu^{3+} REs incubation (**Fig. 5B**). And no obvious luminescence intensity changes were observed between the PAA-coated $KGdF_4$:Eu^{3+} REs (**Fig. 5C**) and the RGD-conjugated $KGdF_4$:Eu^{3+} REs (**Fig. 5D**) in the control H1299 cells. Z scanning analysis showed the luminescence signals of both PAA- and RGD- conjugated $KGdF_4$:Eu^{3+} REs

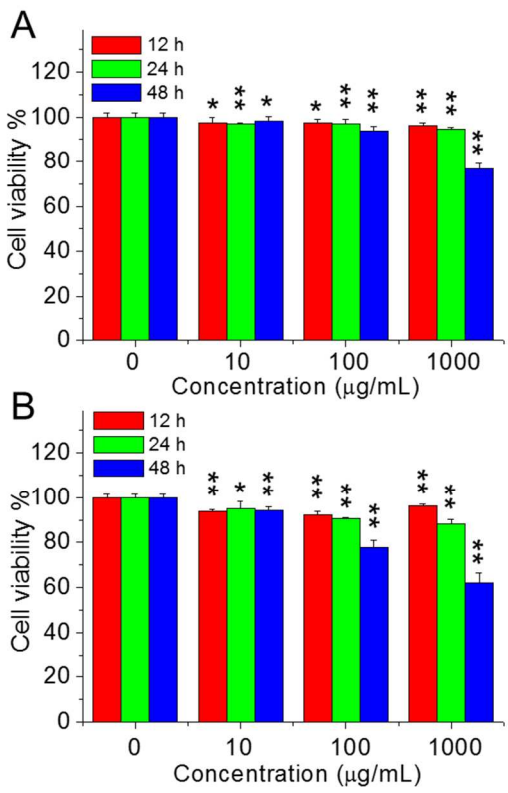

Fig. 4 Viability values (%) of the H1299 cells (**A**) and U87MG cells (**B**) estimated by CCK-8 assay versus incubation concentrations of the PAA-coated $KGdF_4$ REs. Data represent mean +s.d. (n = 6). ∗ $p < 0.05$ compared with control group. ∗∗ $p < 0.01$ compared with control group.

were mainly observed in the perinuclear cytoplasm region of the H1299 cells (**Fig. S7**).

Fluorine–18 (^{18}F) is often used for PET imaging due to its ease in production in high quantities on a medical cyclotron and an ideal half–life of about 110 min, but its labelling reaction generally requires multiple synthetic steps often under harsh conditions and tedious purification processes.[29-31] Recently, the reaction between fluoride and rare-earth metal ions has been applied to label REs with $^{18}F^-$.[10-13] Therefore, $^{18}F^-$ was chosen to label PAA-coated $KGdF_4:Eu^{3+}$ REs for PET imaging. ^{18}F-labeling was carried out by simply mixing [^{18}F]KF solution with aqueous solutions of $KGdF_4$ REs at room temperature followed by 10 min incubation, and free $^{18}F^-$ was easily removed by centrifugation. The ^{18}F-labeling yield for $KGdF_4$ REs was estimated to be ~50%. At the same condition, the ^{18}F-labeling yield for the large size $NaYF_4$ REs with an average diameter of ~25 nm (**Fig. S8**) was ~80%, which is higher than that for the sub-5 nm $KGdF_4$ REs.

For *in vivo* imaging studies, athymic nude mice bearing a U87MG or H1299 tumor on the left shoulder (stomach position) were administered the ^{18}F-labeled $KGdF_4$ REs (~60 μCi/2.22 MBq) through tail-vein injection. At 1 h after injection, the mice were imaged using MicroPET/CT imaging system. Strong uptake of [^{18}F]$KGdF_4$ REs in the lung could be clearly visualized (**Fig. 6**), indicating the aggregation of some sub-5 nm $KGdF_4$ REs. Long-time and high-speed centrifuge may lead to the aggregation of sub-5 nm $KGdF_4$ REs in the purification process of removing the free $^{18}F^-$. At the same condition, nearly no uptake in the lung of mice was obtained for the large size $NaYF_4$ REs (~25 nm) from the MicroPET/CT imaging (**Fig. S9**). These data indicated that small size REs are more likely to aggregate than large size REs.

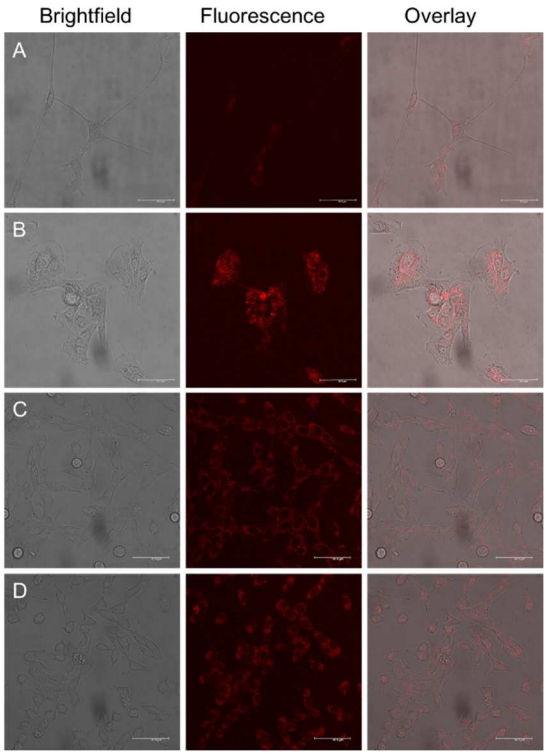

Fig. 5 Fluorescence imaging of live U87MG cells (**A, B**) and H1299 cells (**C, D**) with the $KGdF_4:Eu^{3+}$ REs (20 μg/mL, 2 h). **A, C,** PAA-coated $KGdF_4:Eu^{3+}$ REs. **B, D,** RGD-conjugated $KGdF_4:Eu^{3+}$ REs. Excitation: 405nm, Emission: 580-630nm. Scale bar: 50 μm.

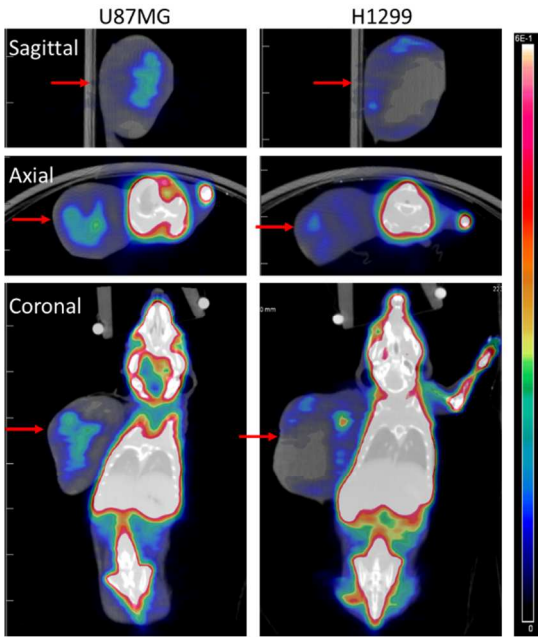

Fig. 6 MicroPET/CT imaging of the U87MG tumor and H1299 tumor bearing mice injected with the [^{18}F]$KGdF_4$ REs (tumors are indicated by red arrows).

The region of interest (ROI) analysis of the U87MG tumor-bearing mouse showed that the mean standardized uptake value (SUV) of [^{18}F]$KGdF_4$ REs in the lung, liver, bladder and bone was 13.6, 2.7, 6.6 and 2.4, respectively. For the H1299 tumor-bearing mouse, the SUV of [^{18}F]$KGdF_4$ REs in the lung, liver, bladder and bone was 7.5, 2.3, 16.3 and 1.7, respectively. In addition, accumulation of the [^{18}F]$KGdF_4$ REs was also visualized in the tumor regions, which is likely due to the enhanced permeability and retention effect. Uptake of the [^{18}F]$KGdF_4$ REs in the U87MG tumor was slightly higher than that in the H1299 tumor. The SUV was 0.13 in the U87MG tumor and 0.085 in the H1299 tumor, respectively.

The accurate amount of $KGdF_4$ REs in the main organs (heart, liver, spleen, lung, kidneys, bone, urine and blood) was measured by ICP-MS analysis (**Fig. S10**). High uptake of the $KGdF_4$ REs was detected in the liver, spleen, lung and blood at 1 h post injection. Slight uptake in the bone and urea was also detected, and the value is lower than that obtained from the SUV result, suggesting that a low level of defluorination of [^{18}F]$KGdF_4$ REs may be occurring *in vivo*. Additionally, the *in vivo* MR imaging was also carried out to support the biodistribution of $KGdF_4$ REs. The pre-contrast and post-contrast T_1-weighted MR images were recorded before and after 1 h injection of 400 uL $KGdF_4$ REs (~ 50 μg). It was noteworthy that the $KGdF_4$ REs could induce an efficient positive-contrast enhancement in the liver, spleen, lung, heart, and kidney (**Fig. S11, Table S1**), which was consistent with the ICP-MS results.

In conclusion, we report sub-5 nm REs based on $KGdF_4$ host as nanoprobes for *in vitro* and *in vivo* imaging. The prepared

$KGdF_4$ REs exhibited the up/down-conversion luminescence by doped Yb^{3+}/Tm^{3+} and Eu^{3+}, respectively. Moreover, these $KGdF_4$ REs showed low cytotoxicity on U87MG and H1299 cells. After conjugating with RGD peptide, these $KGdF_4$ REs were applied to target imaging U87MG cells *in vitro*. In addition, $^{18}F^-$ was labeled with $KGdF_4$ REs for PET imaging, and these $^{18}F^-$ labeled $KGdF_4$ REs were able to imaging U87MG and H1299 tumors in living mice after intravenous injection. To the best of our knowledge, this is the first successful demonstration of sub-5 nm REs for *in vivo* tumor imaging. This study provides a foundation for the development of the whole-body tumor imaging based on the use of ultrasmall REs as multifunctional nanoprobes.

Acknowledgements

This work was supported by grants from the Chinese Natural Science Foundation project (no. 81301261, no. 21374059), the Shanghai Pujiang Project (no. 13PJ1405000), and Doctoral Fund of Ministry of Education of China (no. 20130073120098).

Notes

[a] *School of Biomedical Engineering, Med-X Research Institute, Shanghai Jiao Tong University, Shanghai, 200030, P. R. China. E-mail: xiongliqin@sjtu.edu.cn*

[b] *Department of Nuclear Medicine, Rui Jin Hospital, School of Medicine, Shanghai Jiao Tong University, Shanghai, 200025, P. R. China.*

[c] *Department of Chemistry & The State Key Laboratory of Molecular Engineering of Polymers & Institute of Biomedicine Science, Fudan University, Shanghai, 200433, P. R. China. Email: fyli@fudan.edu.cn*

[d] *Department of Nuclear Medicine, Fudan University Shanghai Cancer Center & Department of Oncology, Shanghai Medical College & Center for Biomedical Imaging, Fudan University, Shanghai, 200032, P. R. China.*

† *Electronic Supplementary Information (ESI) available: [details of the experiment section as well as EDXA, XRD, Zeta potential, FTIR, TGA, stability, TEM, Z scanning, ICP-MS, and MicroPET/CT images]. See DOI: 10.1039/b000000x/*

References

1 J. Zhou, Z. Liu and F. Y. Li, *Chem. Soc. Rev.*, 2012, **41**, 1323–1349.
2 L. Q. Xiong, Z. G. Chen, M. X. Yu, F. Y. Li, C. Liu and C. H. Huang, *Biomaterials,* 2009, **30**, 5592–5600.
3 L. Q. Xiong, Z. G. Chen, Q. W. Tian, T. Y. Cao, C. J. Xu and F. Y. Li, *Anal. Chem.*, 2009, **81**, 8687-8694.
4 F. Wang, Y. Han, C. S. Lim, Y. H. Lu, J. Wang, J. Xu, H. Y. Chen, C. Zhang, M. H. Hong and X. G. Liu, *Nature*, 2010, **463**, 1061–1065.
5 P. Rahman and M. Green, *Nanoscale*, 2009, **1**, 214–224.
6 D. J. Naczynski, M. C. Tan, M. Zevon, B. Wall, J. Kohl, A. Kulesa, S. Chen, C. M. Roth, R. E. Riman and P. V. Moghe, *Nat. Commun.*, 2013, **4**, 2199.
7 S. K. Maji, S. Sreejith, J. Joseph, M. J. Lin, T. C. He, Y. Tong, H. D. Sun, S. W. Yu and Y. L. Zhao, *Adv. Mater.*, 2014, **26**, 5633–5638.
8 D. J. Naczynski, M. C. Tan, R. E. Riman and P. V. Moghe, *J. Mater. Chem. B*, 2014, **2**, 2958-2973.
9 D. J. Naczynski, C. Sun, S. Türkcan, C. Jenkins, A. L. Koh, D. Ikeda, G. Pratx and L. Xing, *Nano Lett.*, 2015, **15**, 96-102.
10 Y. Sun, M. X. Yu, S. Liang, Y. J. Zhang, C. G. Li, T. T. Mou, W. J. Yang, X. Z. Zhang, B. Li, C. H. Huang and F. Y. Li, *Biomaterials*, 2011, **32**, 2999–3007.
11 J. Zhou, M. X. Yu, Y. Sun, X. Z. Zhang, X. J. Zhu, Z. H. Wu, D. M. Wu and F. Y. Li, *Biomaterials*, 2011, **32**, 1148–1156.
12 Q. Liu, Y. Sun, C. G. Li, J. Zhou, C. Y. Li, T. S. Yang, X. Z. Zhang, T. Yi, D. M. Wu and F. Y. Li, *ACS Nano*, 2011, **5**, 3146–3157.
13 L. Q. Xiong, B. Shen, D. Behera, S. S. Gambhir, F. T. Chin and J. H. Rao, *Nanoscale*, 2013, **5**, 3253-3256.
14 R. Li, Z. Ji, J. Dong, C. H. Chang, X. Wang, B. Sun, M. Wang, Y. P. Liao, J. I. Zink, A. E. Nel and T. Xia, *ACS Nano*, 2015, **9**, 3293-3306.
15 L. Cheng, K. Yang, M. W. Shao, X. H. Lu and Z. Liu, *Nanomedicine*, 2011, **6**, 1327-1340.
16 K. Wang, J. B. Ma, M. He, G. Gao, H. Xu, J. Sang, Y. X. Wang, B. Q. Zhao and D. X. Cui, *Theranostics*, 2013, **3**, 258-266.
17 Y. Sun, W. Feng, P. Y. Yang, C. H. Huang and F. Y. Li, *Chem. Soc. Rev.*, 2015, **44**, 1509-1525.
18 Z. J. Gu, L. Yan, G. Tian, S. J. Li, Z. F. Chai and Y. L. Zhao, *Adv. Mater.*, 2013, **25**, 3758-3779.
19 L. Q. Xiong, T. S. Yang, Y. Yang, C. J. Xu and F. Y. Li, *Biomaterials*, 2010, **31**, 7078-7085.
20 H. T. Wong, M. K. Tsang, C. F. Chan, K. L. Wong, B. Fei and J. H. Hao, *Nanoscale*, 2013, **5**, 3465–3473.
21 Q. Ju, D. T. Tu, Y. S. Liu, R. F. Li, H. M. Zhu, J. C. Chen, Z. Chen, M. D. Huang and X. Y. Chen, *J. Am. Chem. Soc.*, 2012, **134**, 1323−1330.
22 P. Tallury, S. Kar, S. Bamrungsap, Y. F. Huang, W. H. Tan and S. Santra, *Chem. Commun.*, 2009, **17**, 2347-2349.
23 E. Phillips, O. Penate-Medina, P. B. Zanzonico, R. D. Carvajal, P. Mohan, Y. P. Ye, J. Humm, M. Gonen, H. Kalaigian, H. Schoder, H. W. Strauss, S. M. Larson, U. Wiesner and M. S. Bradbury, *Sci. Transl. Med.*,2014, **6**, 260ra149/1-10.
24 C. Zhou, M. Long, Y. P. Qin, X. K. Sun and J. Zheng, *Angew. Chem. Int. Ed.*, 2011, **50**, 3168-3172.
25 Z. Li, Q. Sun, Y. A. Zhu, B. E. Tan, Z. P. Xu and S. X. Dou, *J. Mater. Chem. B*, 2014, **2**, 2793-2818.
26 H. T. Wong, F. Vetrone, R. Naccache, H. L. W. Chan, J. H. Hao and J. A. Capobianco, *J. Mater. Chem.*, 2011, **21**, 16589–16596.
27 L. Q. Xiong, M. X. Yu, M. J. Cheng, M. Zhang, X. Y. Zhang, C. J. Xu and F. Y. Li*, Mol. BioSyst.*, 2009, **5**, 241–243.
28 L. Q. Xiong, A. J. Shuhendler and J. H. Rao, *Nat. Commun.,* 2012, **3**, 1193.
29 T. Poethko, M. Schottelius, G. Thumshirn, U. Hersel, M. Herz, G. Henriksen, H. Kessler, M. Schwaiger and H. J. Wester, *J. Nucl. Med.,* 2004, **45**, 892–902.
30 W. B. Cai, X. Z. Zhang, Y. Wu and X. Y. Chen, *J. Nucl. Med.,* 2006, **47**, 1172–1180.
31 N. K. Devaraj, E. J. Keliher, G. M. Thurber, M. Nahrendorf and R. Weissleder, *Bioconjug. Chem.*, 2009, **20**, 397–401.